Fourier-Based Imaging for Subsampled Multistatic Arrays

Yuri Álvarez, Yolanda Rodriguez-Vaqueiro, Borja Gonzalez-Valdes, Fernando Las-Heras, and Antonio García-Pino

***Abstract*—This contribution focuses on the limitations of Fourier-based imaging when applied to subsampled arrays used in multistatic millimeter-wave radar systems. The aim is to determine the relationship between the size of the object under test (OUT), its position with respect to the radar aperture, and the sampling requirements on the aperture so as to recover aliasing-free images. Based on the analysis results, a method for recovering spectral information is proposed, the idea of which is to replicate the plane wave spectrum, and then apply a band-pass filter defined by *a priori* knowledge of the OUT size. For simplicity, the analysis is done in two-dimensional (2-D; range and cross-range dimensions). A simulation-based application is presented for validation purposes.**

***Index Terms*—Backpropagation, fast Fourier transform (FFT), imaging systems, multistatic radar system, sparse array.**

I. Introduction

In the area of homeland security, there is an increasing demand for methods to improve personnel screening for concealed objects and contraband detection at security checkpoints. In this context, active near-field millimeter-wave (mm-wave) imaging radar systems are able to provide high-resolution imaging, with a good tradeoff between accuracy and cost. With the mm-wave radar, the object of interest is first illuminated by millimeter waves, and then the scattered field is measured and processed to reconstruct the surface (or volume) of the object [1]–[3]. The most common mm-wave portal imaging systems currently used are based on monostatic radar and Fourier inversion [3], [4]. The limitations of monostatic imaging systems are mainly related to the appearance of the reconstructed artifacts, as described in [5]. Therefore, bistatic [6], [7] or multistatic systems [1], [8], [9] seem to represent an interesting alternative toward improving personnel imaging.

State-of-the-art mm-wave scanners take advantage of sparse arrays to reduce the number of elements; hence, the technical and economic costs of the scanner [1], [8], [10]. Moreover, the scanning time is also reduced, allowing for real-time image acquisition.

In [1] and [8], the system capability to handle subsampled arrays is shown, assuming that the object under test (OUT) is centered with respect to the scanning system. The next step in the development of security screening systems is on-the-move imaging [11], in which a person (the OUT) can be screened without him or her having to stop in front of the scanner, taking advantage of the movement of the person through a hallway to obtain multistatic views. In this way, multiple oblique angles of incidence and reception are obtained due to the diverse relative positions of the person with respect to the antennas.

Fourier-based imaging developed in [5] for multistatic setups allows fast, real-time image generation. This communication describes the issues that arise when Fourier-based imaging is applied to a multistatic mm-wave imaging system architecture, e.g., the one that is proposed in [11] in which the person under test is off-centered with respect to the radar system. A technique to partially recover the information that may be lost due to the particular spectral properties of subsampled multistatic arrays is proposed.

Manuscript received July 14, 2015; revised February 23, 2016; accepted March 25, 2016. Date of publication XXXX XX, XXXX; date of current version XXXX XX, XXXX. This work was supported in part by the Ministerio de Economía y Competitividad, Gobierno de España, National Research and Development Program under Projects TEC2011-28683-C02-02, TEC 2014-54005-P (“MIRIIEM”), TEC 2014-55290-JIN (“PORTEMVISION”), and Terasense CSD2008-00068 (Consolider-Ingenio 2010); in part by the Spanish Government under Project TACTICA; in part by the European Regional Development Fund (FEDER); in part by the Galician Regional Government under projects CN2012/279, CN2012/260 (AtlantTIC), and Plan I2C (2011–2015); and in part by the Gobierno del Principado de Asturias under project GRUPIN14-114.

Y. Álvarez and F. Las-Heras are with the Department of Electrical Engineering, Universidad de Oviedo, Gijón E-33203, Spain (e-mail: yalopez@tsc.uniovi.es; flasheras@tsc.uniovi.es).

Y. Rodriguez-Vaqueiro, B. Gonzalez-Valdes, and A. García-Pino are with the AtlantTIC Research Center, Universidad de Vigo, Vigo E-36310, Spain (e-mail: bgvaldes@com.uvigo.es; yrvaqueiro@com.uvigo.es; agpino@com.uvigo.es).

Color versions of one or more of the figures in this communication are available online at http://ieeexplore.ieee.org.

Digital Object Identifier 10.1109/TAP.2016.2550035

II. Multistatic Imaging

Multistatic imaging considers different propagation paths for the incident and scattered fields, unlike monostatic imaging, in which these paths are the same. For simplicity, a two-dimensional (2-D) space is considered. The definition of the coordinate system is as follows: the *x*-axis represents the cross-range dimension, and the *y*-axis is the range axis (depth).

Given the reflectivity function of an object $\rho(x', y')$, the field scattered on a flat receiving aperture located at $y = Y_0, E_{scatt}\ (x, f)$ is given by

$$E_{scatt}(x,f) = \int\limits_{x'}\int\limits_{y'} \left\{ \begin{array}{l} \rho(x',y') \cdot e^{-jk(\,(x-x')^2+(Y_0-y')^2)^{1/2}} \cdot \\ e^{-jk(\,(x_{inc}-x')^2+(y_{inc}-y')^2)^{1/2}} \end{array} \right\} dy'dx' \tag{1}$$

where $(x_{\text{inc}}, y_{\text{inc}})$ is the position of the transmitter, which is considered to be a point source, and $k = 2\pi/\lambda = 2\pi f/c$.

Note that the scattered field is a complex signal; thus, its plane wave spectrum is nonsymmetric. Equation (1) can be inverted to recover the reflectivity function from the scattered field samples collected at a certain frequency bandwidth, yielding the well-known SAR backpropagation imaging equation [7], [9]

$$\rho(x',y') = \int\limits_{x}\int\limits_{f} \left\{ \begin{array}{l} E_{scatt}(x,f) \cdot e^{+jk(\,(x-x')^2+(Y_0-y')^2)^{1/2}} \cdot \\ e^{+jk(\,(x_{inc}-x')^2+(y_{inc}-y')^2)^{1/2}} \end{array} \right\} df\,dx. \tag{2}$$

Equation (2) can be solved by means of Fourier-based imaging, as explained in [5]. The basic idea is to use the Fourier transform property that states that a displacement in the spatial domain is equivalent to a phase shift in the frequency domain. Fourier-based imaging is faster than directly solving (2) because fast implementations, such as FFT and IFFT, are available. Additionally, the Nyquist sampling criterion, which sets a limitation on the minimum number of array elements to ensure aliasing-free recovered images, needs to be fulfilled, as described in detail in the following paragraphs. A monochromatic approach (i.e., single-frequency analysis) is assumed.

Consider the imaging setup presented in Fig. 1(a), which consists of a linear array of receivers parallel to the *x*-axis and a single transmitter. In this case, the OUT is centered with respect to the receiving array, which is within a $\pm\theta_{\text{obj}}$ angle. The plane wave spectrum can be expected to have incident directions ranging from $-\theta_{\text{obj}}$ to $+\theta_{\text{obj}}$, i.e., in the angular region where the OUT is situated. It should be noted that

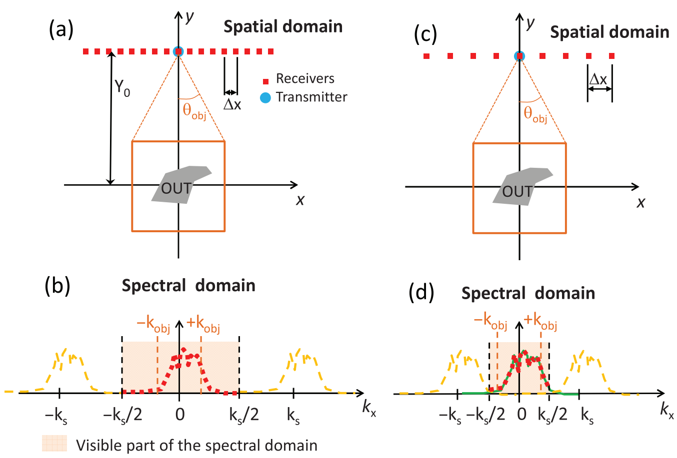

Fig. 1. (a) Imaging setup: linear array of receivers and point source-like transmitter; the OUT is centered with respect to the receiving array. (b) Spectral domain: the visible part of the scattered field plane wave spectrum (red dotted line) and the spectrum replicas (yellow dashed line) are shown. (c) Imaging setup when the spacing between samples is increased. (d) Plane wave spectrum of the OUT (green line). Due to the increased separation between receivers, the visible part of the spectrum is shortened (red dotted line).

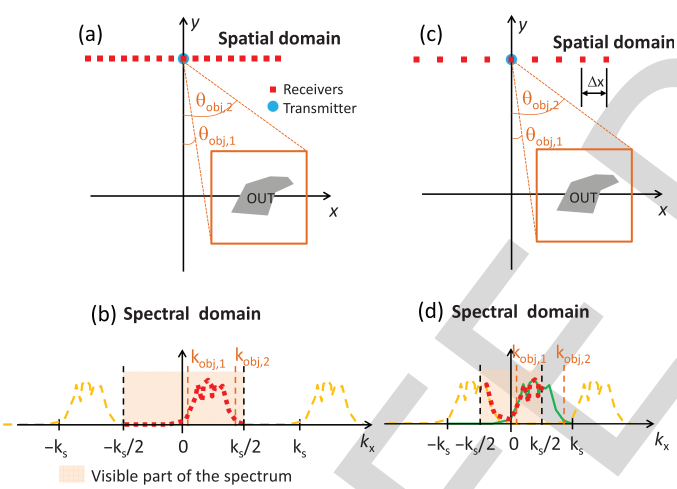

Fig. 2. (a) Imaging setup when the OUT is off-centered with respect to the receiving array. (b) Spectral domain. (c) Imaging setup when the receiving array is subsampled. (d) Spectral domain: part of the scattered field plane wave spectrum (green line) lies outside the visible part of the spectrum $[-k_s/2\ k_s/2]$.

the approach that considers all the plane wave contributions as within the range $[-\theta_{obj}\ \theta_{obj}]$ is based on *a priori* knowledge of the OUT size. It does not take into account the OUT geometry (the unknown in the imaging problem), which, due to protrusions or bumps, can create a scattered field with plane wave components outside the $[-\theta_{obj}\ \theta_{obj}]$ interval.

Next, the plane wave spectrum k_x for a single frequency is shown in Fig. 1(b). If the receivers are placed every Δx, then the sampling frequency in the k_x domain is $k_s = 2\pi/\Delta x$. Thus, if $\Delta x = \lambda/2$, then $k_s = 4\pi/\lambda = 2k$. The spectrum replicas [Fig. 1(b), yellow dashed line] are centered at $\pm n k_s$, with $n = 1, 2, \ldots$. The plane wave coefficient associated with the incident direction θ_{obj} is given by $k_{obj} = k\sin(\theta_{obj})$.

Fig. 1(c) presents the spatial domain when the separation between receivers (Δx) increases with respect to the previous case. Therefore,

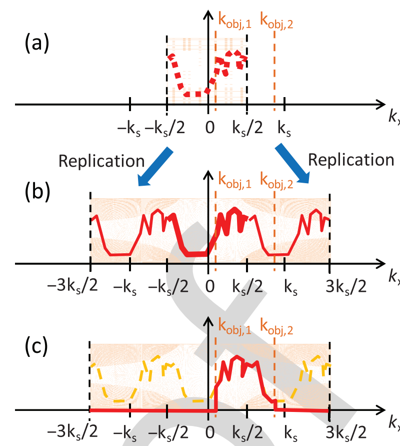

Fig. 3. (a) Plane wave spectrum in the visible $[-k_s/2\ k_s/2]$ interval. (b) Plane wave spectrum replication on the left and right. (c) Plane wave spectrum filtering within the $[k_{obj,1}\ k_{obj,2}]$ interval.

the spectral domain [Fig. 1(d)] is compressed, which may cause overlapping between spectral replicas.

III. Fourier-Based Imaging for Off-Centered OUT

As stated in Section I, on-the-move personnel screening has to take into account cases in which the OUT is not centered with respect to the receiving array, as shown in Fig. 2(a). Such cases include, e.g., those in which the person is on one side of the system.

In this case, the field of view ranges from $\theta_{obj,1}$ to $\theta_{obj,2}$. In the spectral domain k_x, the values of $k_{obj,1}$ and $k_{obj,2}$ are given by the position of the OUT with respect to the center of the receiving array. Thus, the scattered field plane wave coefficients are within the range $k_{obj,1} = k\sin(\theta_{obj,1})$ to $k_{obj,2} = k\sin(\theta_{obj,2})$, as plotted in Fig. 2(b).

Provided that the receiving array is sampled below the Nyquist criterion, $\Delta x \leq \lambda/2$, even for a limiting case with $\theta_{obj,i} = 90^\circ (i = 1,2)$, $k_s/2 \geq k_{obj,i} = k$, and no aliasing will occur.

When $\Delta x > \lambda/2$, the array is subsampled, as shown in Fig. 2(c). If $\Delta x > \pi/(k\sin(\theta_{obj,i})) = \lambda/(2\sin(\theta_{obj,i}))$, then part of the OUT plane wave spectrum will be outside the spectral interval $-k_s/2$ to $k_s/2$, as presented in Fig. 2(d). This means that spectral information will be lost, and the OUT will not be correctly reconstructed. Besides, the adjacent spectral replicas partially lie within the $[-k_s/2 k_s/2]$ interval, as shown in Fig. 2(d) (yellow dashed line).

A new method to recover the information within the interval $[k_{obj,1}\ k_{obj,2}]$ is proposed for cases in which only nonsignificant parts of the spectrum overlap, as plotted in Fig. 2(d). The proposed technique of spectral information recovery consists of three steps, as presented in Fig. 3.

1) From the acquired scattered field, the plane wave spectrum between $[-k_s/2\ k_s/2]$ is calculated [Fig. 3(a)].
2) Because the limits $k_{obj,1}$ and $k_{obj,2}$ are known from the estimated OUT size, the plane wave spectrum is replicated n times (with $n > 0$) on the left and the right side [Fig. 3(b)], satisfying $(-2n-1)k_s/2 < [k_{obj,1}\ k_{obj,2}] < (2n+1)k_s/2$.
3) Finally, a band-pass filter is applied such that only the plane wave spectrum within the $[k_{obj,1}\ k_{obj,2}]$ interval, i.e., the relevant plane wave coefficients for OUT imaging, is maintained [Fig. 3(c)]. The reconstructed image of the OUT is created with the data associated with the filtered plane wave spectrum coefficients.

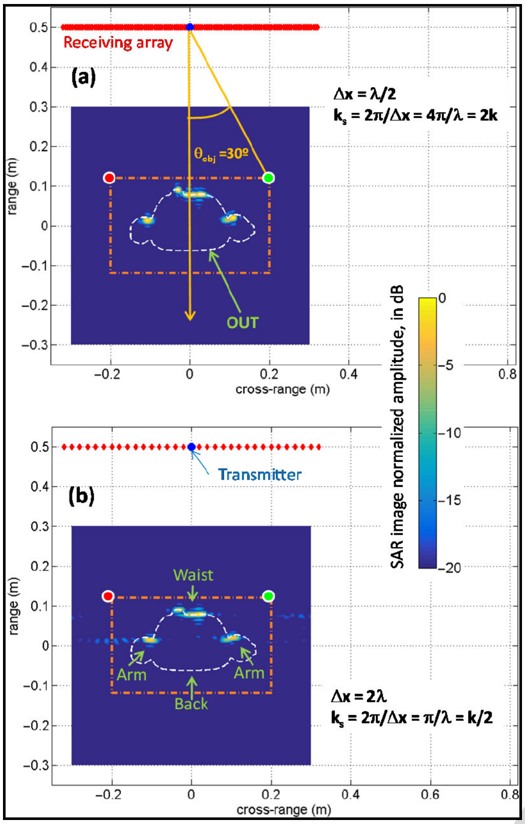

Fig. 4. Setup for mm-wave imaging with a linear receiving array and a point source-like transmitter. The OUT (white dashed line) is centered with respect to the receiving array. (a) Receiving array sampled every $\lambda/2$. (b) Receiving array sampled every 2λ.

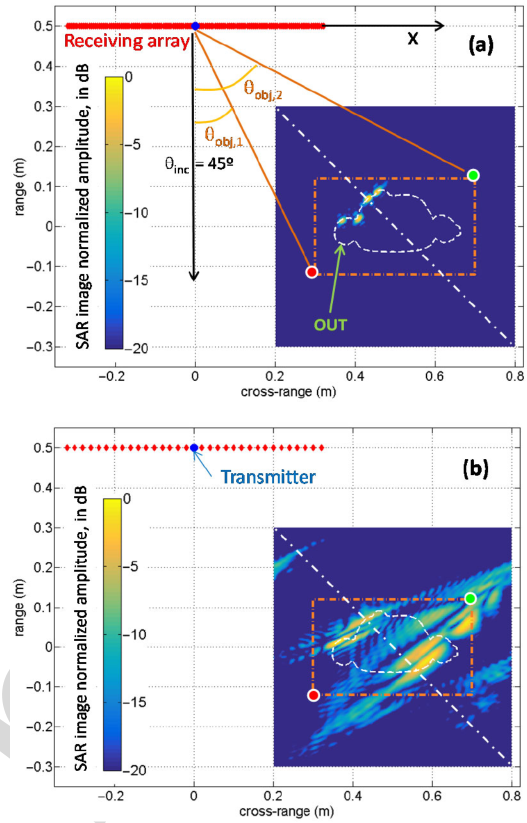

Fig. 6. Setup for mm-wave imaging with a linear receiving array and a point source-like transmitter. The OUT (white dashed line) is displaced 50 cm along the cross-range axis with respect to the receiving array. (a) Receiving array sampled every $\lambda/2$. (b) Receiving array sampled every 2λ.

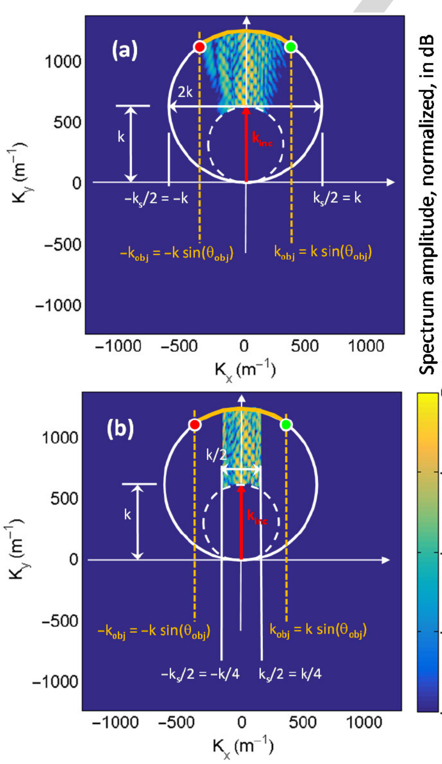

Fig. 5. Plane wave spectrum of the scattered field when the OUT is centered with respect to the receiving array. (a) Receiving array sampled every $\lambda/2$. (b) Receiving array sampled every 2λ.

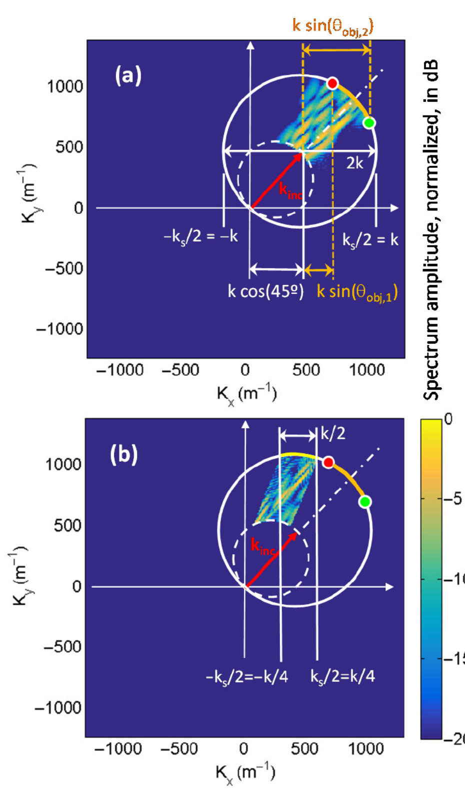

Fig. 7. Plane wave spectrum of the scattered field when the OUT is displaced 50 cm along the x-axis with respect to the receiving array. (a) Receiving array sampled every $\lambda/2$. (b) Receiving array sampled every 2λ.

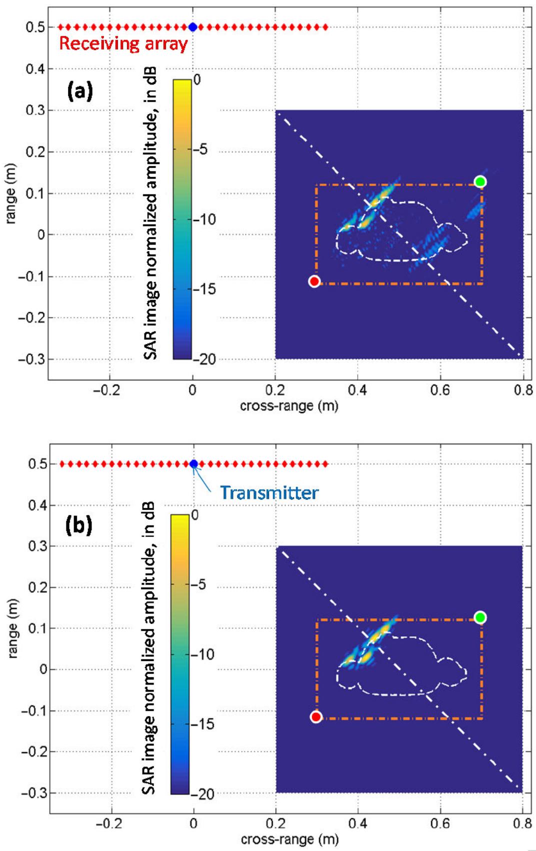

Fig. 8. Setup for mm-wave imaging with a linear receiving array sampled every 2λ and a point source-like transmitter. The OUT (white dashed line) is displaced 50 cm along the cross-range axis with respect to the receiving array. SAR imaging results (a) after spectrum replication and (b) after spectrum replication and filtering.

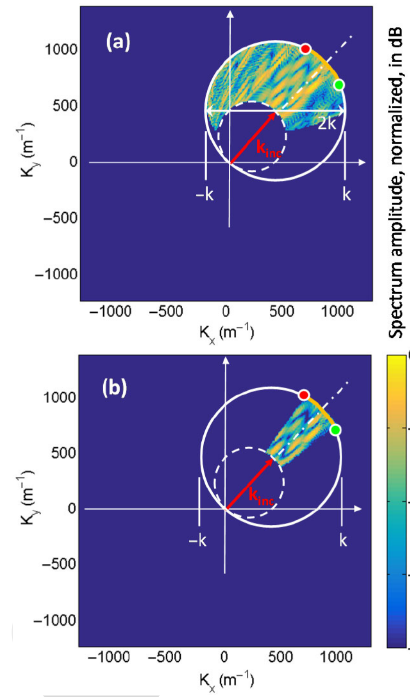

Fig. 9. Plane wave spectrum of the scattered field when the OUT is displaced 50 cm along the x-axis with respect to the receiving array. (a) After spectrum replication. (b) After spectrum replication and filtering.

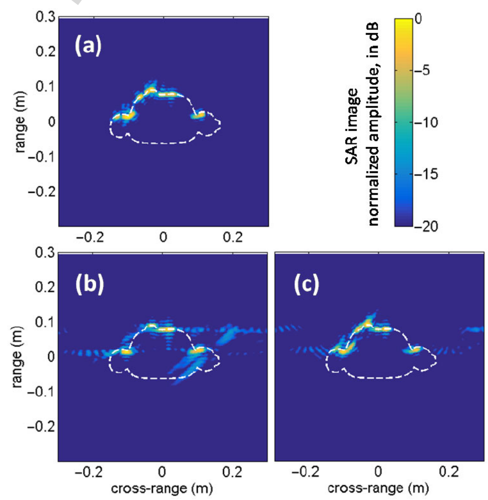

Fig. 10. Combined centered and off-centered SAR images. (a) Receiving array sampled every $\lambda/2$. (b) Receiving array sampled every 2λ. (c) Receiving array sampled every 2λ, applying spectrum replication and filtering.

IV. Application Example

The described methodology is validated through a simulation-based application example. The scattered field is simulated by using the 2-D method-of-moments MATLAB code, which implements electric field integral equations [12].

Fig. 4 presents the imaging setup, which resembles a typical mm-wave imaging system for screening applications: the OUT represents a person's cross-section with an object on the waist. A point source-like transmitter provides illumination, and a linear array of receivers collects the scattered field. Vertical (TM) polarization is considered, with a 15–30 GHz working frequency band.

As described in [11], an on-the-move imaging system takes advantage of the multiple positions of a person to recover the entire profile. To show this concept, two different OUT positions, centered and off-centered with respect to the receiving array, are considered in this example.

For the case in which the OUT is facing the receiving array, the viewing angle is $\theta_{\text{obj}} \leq 30°$.

Fig. 4 presents the imaging results for array sampling rates of $\lambda/2$ [Fig. 4(a)] and 2λ [Fig. 4(b)] at $f = 30$ GHz. The latter image is slightly distorted due to aliasing. The plane wave spectra for these two cases are plotted in Fig. 5(a) and (b), respectively. The correspondence between the spatial and the spectral mapping for the extreme angles $\pm\theta_{\text{obj}}$ are denoted by red (●) and green (●) circles, respectively, in Figs. 4 and 5.

For the k_x and k_y coordinates, the k-space mapping is given by [3], [5]

$$k_x = \underbrace{k\sin(\theta_{inc})}_{k_{x,inc}} + k\sin(\theta_{\text{obj}}) \tag{3}$$

$$k_y = \underbrace{k\cos(\theta_{inc})}_{k_{y,inc}} + \sqrt{k^2 - (k\sin(\theta_{\text{obj}}))^2}. \tag{4}$$

The terms $k_{\text{x,inc}}$ and $k_{\text{y,inc}}$ refer to the incident field compensation, with θ_{inc} denoting the incident field angle with respect to the y-(range) axis ($\theta_{\text{inc}} = 0°$ in this case). Multistatic imaging requires that the plane

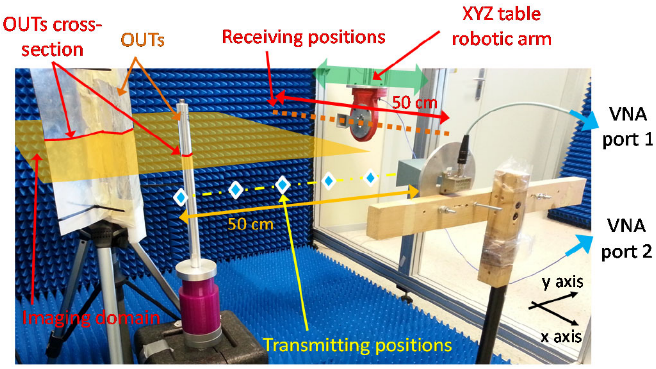

Fig. 11. Ku-band measurement setup for experimental validation. The receiver is mounted on a robotic arm and the transmitter is manually placed at six different positions. The transmitting horn antenna is connected to Port 1 of the vector network analyzer (VNA), and the receiving horn antenna, mounted on the XYZ table robotic arm, to Port 2 of the VNA. Vertical polarization is considered.

wave spectrum be compensated by the incident field. For simplicity, the spherical wave of the incident field can be locally approximated as a plane wave [5]; thus, in the spectral domain, the incident field compensation is a linear shift with magnitude $k_{\mathrm{inc}} = k$ (Fig. 7, red arrow).

When the array is sampled every $\lambda/2$, then $k_s/2 = k$, as shown in Fig. 5(a). In this case, $k_{\mathrm{obj}} = k\sin(30^\circ) = k/2 < k_s/2$. When the distance between consecutive receivers is 2λ, the sampling rate increases according to $k_s/2 = k/4$ [Fig. 5(b)], and $k_{\mathrm{obj}} = k/2 > k_s/2$. This will cause the spectral replicas to overlap and the OUT image to become distorted due to aliasing.

Next, the OUT is displaced 50 cm in the x-direction, as shown in Fig. 6. For a receiving array separation of $\lambda/2$ [Fig. 6(a)], the image does not suffer from aliasing because $k_s/2 = k > \max([k_{\mathrm{obj},1} k_{\mathrm{obj},2}])$. Fig. 7(a) shows the analysis results for this case in the spectral domain. The incident field can be approached by a $\theta_{\mathrm{inc}} = 45^\circ$ incident plane wave; thus, the plane wave spectrum is shifted to $k_{x,\mathrm{inc}} = k\cos(45^\circ)$ and $k_{y,\mathrm{inc}} = k\sin(45^\circ)$ [5]. The correspondence between the spatial and the spectral mapping for the extreme angles $\theta_{\mathrm{obj},1}$ and $\theta_{\mathrm{obj},2}$ are indicated by red (●) and green (●) circles, respectively, in Figs. 6 and 7.

If the sampling rate is lowered to $k_s/2 = k/4$, then the spectral domain will be outside the $[k_{\mathrm{obj},1} k_{\mathrm{obj},2}]$ interval, as shown in Fig. 7(b). As a result, the OUT cannot be imaged, as plotted in Fig. 6(b).

To recover the plane wave spectrum, the methodology presented in Fig. 3 is applied. First, the plane wave spectrum in the $[-k_s/2\ k_s/2]$ interval is replicated twice on the left and twice on the right to cover the $[-5k_s/2 5k_s/2]$ range. After applying the corresponding incident field compensation (k_{inc}), the extended plane wave spectrum is plotted in Fig. 9(a). Now, the condition $-5k_s/2 < [k_{\mathrm{obj},1} k_{\mathrm{obj},2}] < 5k_s/2$ is satisfied. Due to the spectral replicas, the recovered OUT image suffers from aliasing, as shown in Fig. 8(a).

To remove the plane wave spectrum replicas, the band-pass filter $[k_{\mathrm{obj},1}\ k_{\mathrm{obj},2}]$ is applied to the spectral domain [Fig. 9(b)]. Although it is not possible to remove aliasing completely, it should be noted that the main features visible in Fig. 6(a) are also present in the recovered image in Fig. 8(b).

Concerning the practical application of the proposed method to an on-the-move imaging system, the images for different OUT positions can be combined as described in [11] to recover the OUT profile. In this case, only two positions are tested; the results are plotted in Fig. 10. In the case of subsampled arrays, although aliasing cannot be fully removed, the proposed technique allows for accurate OUT profile reconstruction with a reduced number of receiving elements, thus making the mm-wave imaging system simpler in terms of technical and economic effort.

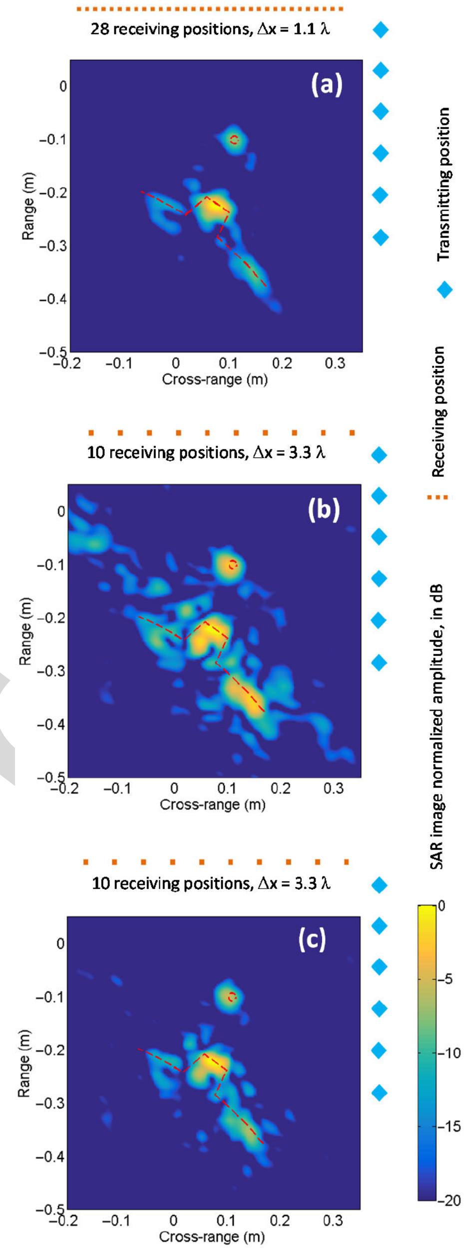

Fig. 12. Combined centered and off-centered SAR images. (a) Receiving array sampled every 1.1λ at 18 GHz. (b) Receiving array sampled every 3.3λ. (c) Receiving array sampled every 3.3λ, applying spectrum replication and filtering. Red dashed line represents the true OUTs profile.

V. Measurements Results

The imaging setup described in Section IV is replicated inside an XYZ table measurement range [13] for practical validation with measurements in the Ku frequency band (12–18 GHz). Fig. 11 shows a picture of the measurement setup. In this setup, the transmitting and receiving positions are located along different sides of the imaging domain, as shown in Figs. 11 and 12, aiming to test the capability of the proposed technique to work with this kind of multistatic imaging setups [5].

Scattered field is measured along a linear synthetic aperture placed at $y = +0.5$ m, ranging from $x = -0.2$ m to $x = +0.3$ m. Six equally spaced transmitting positions, placed at $x = 0.5$ m, and ranging from $y = -0.3$ m to $y = +0.2$ m are considered. The OUTs are a bent metallic plate resembling the cross-section of a human body torso with an object on it, and a 2-cm diameter metallic pole placed at $x = 0.1$ cm, $y = -0.1$ cm, used also as a reference for optical alignment of the transmitter when manually moved from one position to another.

The same process described in Section IV is applied to the measured field samples for every transmitting position. Fig. 12 presents the combined SAR images for all the transmitting positions. Even with a subsampling of 1.1λ [28 receiving positions, Fig. 12(a)] OUTs profile can be recovered without aliasing. However, when the subsampling is increased up to 3.3λ [10 receiving positions, Fig. 12(b)], the recovered image is distorted by aliasing, which can be partially removed after the application of spectrum replication and filtering [Fig. 12(c)].

VI. Conclusion

The limitations of Fourier-based imaging applied to multistatic systems with subsampled arrays were presented and discussed, and a simple technique for partial recovery of plane wave spectrum information was introduced. The simulation and measurement results confirm the viability of the proposed approach in the development of on-the-move multistatic mm-wave imaging systems or any other radar configuration in which the target is off-centered.

References

[1] S. S. Ahmed, A. Schiessl, F. Gumbmann, M. Tiebout, S. Methfessel, and L. Schmidt, "Advanced microwave imaging," *IEEE Microw. Mag.*, vol. 13, no. 6, pp. 26–43, Sep./Oct. 2012.

[2] S. S. Ahmed, "Personnel screening with advanced multistatic imaging technology," in *Proc. SPIE Defense Secur. Sens. Int. Soc. Opt. Photonics*, 2013.

[3] D. M. Sheen, D. L. McMakin, and T. E. Hall, "Three-dimensional millimeter-wave imaging for concealed weapon detection," *IEEE Trans. Microw. Theory Techn.*, vol. 49, no. 9, pp. 1581–1592, Sep. 2001.

[4] D. M. Sheen, D. L. McMakin, and T. E. Hall, "Combined illumination cylindrical millimeter-wave imaging technique for concealed weapon detection," in *Proc. AeroSense Int. Soc. Opt. Photonics*, Jul. 2000, pp. 52–60.

[5] Y. Álvarez *et al.*, "Fourier-based imaging for multistatic radar systems," *IEEE Trans. Microw. Theory Techn.*, vol. 62, no. 8, pp. 1798–1810, Aug. 2014.

[6] G. Yates, M. Horne, A. Blake, R. Middleton, and D. Andre, "Bistatic SAR image formation," *IEE Proc. Radar Sonar Navig.*, vol. 153, no. 3, pp. 208–213, 2006.

[7] M. Soumekh, "Bistatic synthetic aperture radar inversion with application in dynamic object imaging," *IEEE Trans. Signal Process.*, vol. 39, no. 9, pp 2044–2055, Sep. 1991.

[8] X. Zhuge and A. G. Yarovoy, "A sparse aperture MIMO-SAR-based UWB imaging system for concealed weapon detection," *IEEE Trans. Geosci. Remote Sens.*, vol. 49, no. 1, pp. 509–518, Jan. 2011.

[9] B. Gonzalez-Valdes, Y. Alvarez, J. A. Martinez, F. Las-Heras, and C. M. Rappaport, "On the use of improved imaging techniques for the development of a multistatic three-dimensional millimeter-wave portal for personnel screening," *Progr. Electromagn. Res.*, vol. 138, pp. 83–98, 2013.

[10] Y. Rodríguez-Vaqueiro, Y. Álvarez, B. Gonzalez-Valdes, J. A. Martínez-Lorenzo, F. Las-Heras, and C. M. Rappaport, "On the use of compressed sensing techniques for improving multistatic millimeter-wave portal-based personnel screening," *IEEE Trans. Antennas Propag.*, vol. 62, no. 1, pp. 494–499, Jan. 2014.

[11] B. Gonzalez-Valdes, C. Rappaport, and J. A. Martinez-Lorenzo, "On-the-move active millimeter wave interrogation system using a hallway of multiple transmitters and receivers," in *Proc. IEEE Int. Symp. Antennas Propag.*, Memphis, TN, USA, Jul. 6–11, 2014, pp. 1107–1108.

[12] C. A. Balanis, *Advanced Engineering Electromagnetics*. Hoboken, NJ, USA: Wiley, 1989.

[13] A. Arboleya, Y. Alvarez, and F. Las-Heras, "Millimeter and submillimeter planar measurement setup," in *Proc. IEEE Antennas Propag. Soc. Int. Symp. (APS-URSI)*, Orlando, FL, USA, Jul. 7–13, 2013, pp. 1–2.

QUERIES

Q1: Please confirm whether the edit made in the sentence “This communication...” is correct.
Q2: Please provide page range for Ref. [2].

Fourier-Based Imaging for Subsampled Multistatic Arrays

Yuri Álvarez, Yolanda Rodriguez-Vaqueiro, Borja Gonzalez-Valdes, Fernando Las-Heras, and Antonio García-Pino

***Abstract*—This contribution focuses on the limitations of Fourier-based imaging when applied to subsampled arrays used in multistatic millimeter-wave radar systems. The aim is to determine the relationship between the size of the object under test (OUT), its position with respect to the radar aperture, and the sampling requirements on the aperture so as to recover aliasing-free images. Based on the analysis results, a method for recovering spectral information is proposed, the idea of which is to replicate the plane wave spectrum, and then apply a band-pass filter defined by *a priori* knowledge of the OUT size. For simplicity, the analysis is done in two-dimensional (2-D; range and cross-range dimensions). A simulation-based application is presented for validation purposes.**

***Index Terms*—Backpropagation, fast Fourier transform (FFT), imaging systems, multistatic radar system, sparse array.**

I. Introduction

In the area of homeland security, there is an increasing demand for methods to improve personnel screening for concealed objects and contraband detection at security checkpoints. In this context, active near-field millimeter-wave (mm-wave) imaging radar systems are able to provide high-resolution imaging, with a good tradeoff between accuracy and cost. With the mm-wave radar, the object of interest is first illuminated by millimeter waves, and then the scattered field is measured and processed to reconstruct the surface (or volume) of the object [1]–[3]. The most common mm-wave portal imaging systems currently used are based on monostatic radar and Fourier inversion [3], [4]. The limitations of monostatic imaging systems are mainly related to the appearance of the reconstructed artifacts, as described in [5]. Therefore, bistatic [6], [7] or multistatic systems [1], [8], [9] seem to represent an interesting alternative toward improving personnel imaging.

State-of-the-art mm-wave scanners take advantage of sparse arrays to reduce the number of elements; hence, the technical and economic costs of the scanner [1], [8], [10]. Moreover, the scanning time is also reduced, allowing for real-time image acquisition.

In [1] and [8], the system capability to handle subsampled arrays is shown, assuming that the object under test (OUT) is centered with respect to the scanning system. The next step in the development of security screening systems is on-the-move imaging [11], in which a person (the OUT) can be screened without him or her having to stop in front of the scanner, taking advantage of the movement of the person through a hallway to obtain multistatic views. In this way, multiple oblique angles of incidence and reception are obtained due to the diverse relative positions of the person with respect to the antennas.

Fourier-based imaging developed in [5] for multistatic setups allows fast, real-time image generation. This communication describes the issues that arise when Fourier-based imaging is applied to a multistatic mm-wave imaging system architecture, e.g., the one that is proposed in [11] in which the person under test is off-centered with respect to the radar system. A technique to partially recover the information that may be lost due to the particular spectral properties of subsampled multistatic arrays is proposed.

Manuscript received July 14, 2015; revised February 23, 2016; accepted March 25, 2016. Date of publication XXXX XX, XXXX; date of current version XXXX XX, XXXX. This work was supported in part by the Ministerio de Economía y Competitividad, Gobierno de España, National Research and Development Program under Projects TEC2011-28683-C02-02, TEC 2014-54005-P ("MIRIIEM"), TEC 2014-55290-JIN ("PORTEMVISION"), and Terasense CSD2008-00068 (Consolider-Ingenio 2010); in part by the Spanish Government under Project TACTICA; in part by the European Regional Development Fund (FEDER); in part by the Galician Regional Government under projects CN2012/279, CN2012/260 (AtlantTIC), and Plan I2C (2011–2015); and in part by the Gobierno del Principado de Asturias under project GRUPIN14-114.

Y. Álvarez and F. Las-Heras are with the Department of Electrical Engineering, Universidad de Oviedo, Gijón E-33203, Spain (e-mail: yalopez@tsc.uniovi.es; flasheras@tsc.uniovi.es).

Y. Rodriguez-Vaqueiro, B. Gonzalez-Valdes, and A. García-Pino are with the AtlantTIC Research Center, Universidad de Vigo, Vigo E-36310, Spain (e-mail: bgvaldes@com.uvigo.es; yrvaqueiro@com.uvigo.es; agpino@com.uvigo.es).

Color versions of one or more of the figures in this communication are available online at http://ieeexplore.ieee.org.

Digital Object Identifier 10.1109/TAP.2016.2550035

II. Multistatic Imaging

Multistatic imaging considers different propagation paths for the incident and scattered fields, unlike monostatic imaging, in which these paths are the same. For simplicity, a two-dimensional (2-D) space is considered. The definition of the coordinate system is as follows: the *x*-axis represents the cross-range dimension, and the *y*-axis is the range axis (depth).

Given the reflectivity function of an object $\rho(x', y')$, the field scattered on a flat receiving aperture located at $y = Y_0, E_{scatt}\ (x, f)$ is given by

$$E_{scatt}(x,f) = \iint_{x'\,y'} \left\{ \begin{array}{l} \rho(x',y') \cdot e^{-jk((x-x')^2+(Y_0-y')^2)^{1/2}} \cdot \\ e^{-jk((x_{inc}-x')^2+(y_{inc}-y')^2)^{1/2}} \end{array} \right\} dy'dx' \quad (1)$$

where $(x_{\text{inc}}, y_{\text{inc}})$ is the position of the transmitter, which is considered to be a point source, and $k = 2\pi/\lambda = 2\pi f/c$.

Note that the scattered field is a complex signal; thus, its plane wave spectrum is nonsymmetric. Equation (1) can be inverted to recover the reflectivity function from the scattered field samples collected at a certain frequency bandwidth, yielding the well-known SAR backpropagation imaging equation [7], [9]

$$\rho(x', y') = \iint_{x\,f} \left\{ \begin{array}{l} E_{scatt}(x,f) \cdot e^{+jk((x-x')^2+(Y_0-y')^2)^{1/2}} \cdot \\ e^{+jk((x_{inc}-x')^2+(y_{inc}-y')^2)^{1/2}} \end{array} \right\} df\,dx. \quad (2)$$

Equation (2) can be solved by means of Fourier-based imaging, as explained in [5]. The basic idea is to use the Fourier transform property that states that a displacement in the spatial domain is equivalent to a phase shift in the frequency domain. Fourier-based imaging is faster than directly solving (2) because fast implementations, such as FFT and IFFT, are available. Additionally, the Nyquist sampling criterion, which sets a limitation on the minimum number of array elements to ensure aliasing-free recovered images, needs to be fulfilled, as described in detail in the following paragraphs. A monochromatic approach (i.e., single-frequency analysis) is assumed.

Consider the imaging setup presented in Fig. 1(a), which consists of a linear array of receivers parallel to the *x*-axis and a single transmitter. In this case, the OUT is centered with respect to the receiving array, which is within a $\pm\theta_{\text{obj}}$ angle. The plane wave spectrum can be expected to have incident directions ranging from $-\theta_{\text{obj}}$ to $+\theta_{\text{obj}}$, i.e., in the angular region where the OUT is situated. It should be noted that

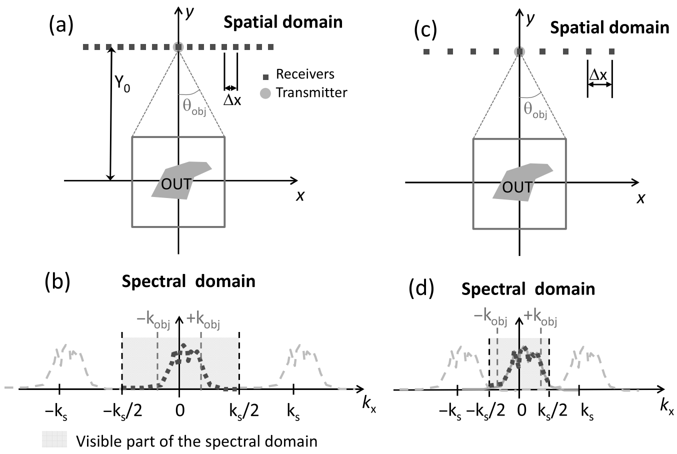

Fig. 1. (a) Imaging setup: linear array of receivers and point source-like transmitter; the OUT is centered with respect to the receiving array. (b) Spectral domain: the visible part of the scattered field plane wave spectrum (red dotted line) and the spectrum replicas (yellow dashed line) are shown. (c) Imaging setup when the spacing between samples is increased. (d) Plane wave spectrum of the OUT (green line). Due to the increased separation between receivers, the visible part of the spectrum is shortened (red dotted line).

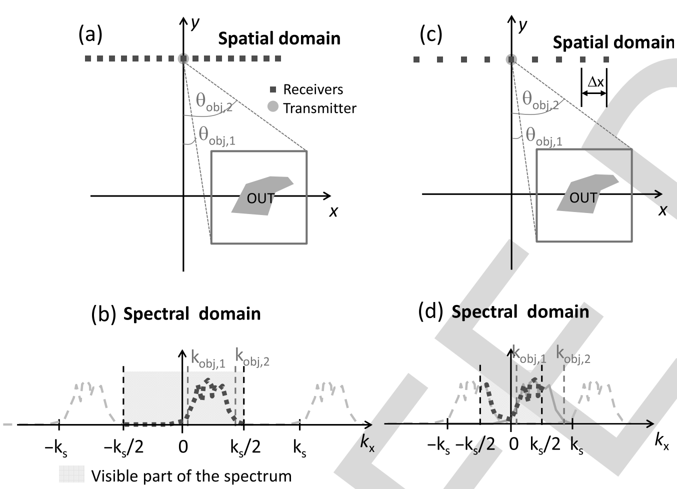

Fig. 2. (a) Imaging setup when the OUT is off-centered with respect to the receiving array. (b) Spectral domain. (c) Imaging setup when the receiving array is subsampled. (d) Spectral domain: part of the scattered field plane wave spectrum (green line) lies outside the visible part of the spectrum $[-k_s/2\ k_s/2]$.

the approach that considers all the plane wave contributions as within the range $[-\theta_{obj}\ \theta_{obj}]$ is based on *a priori* knowledge of the OUT size. It does not take into account the OUT geometry (the unknown in the imaging problem), which, due to protrusions or bumps, can create a scattered field with plane wave components outside the $[-\theta_{obj}\ \theta_{obj}]$ interval.

Next, the plane wave spectrum k_x for a single frequency is shown in Fig. 1(b). If the receivers are placed every Δx, then the sampling frequency in the k_x domain is $k_s = 2\pi/\Delta x$. Thus, if $\Delta x = \lambda/2$, then $k_s = 4\pi/\lambda = 2k$. The spectrum replicas [Fig. 1(b), yellow dashed line] are centered at $\pm n k_s$, with $n = 1, 2, \ldots$. The plane wave coefficient associated with the incident direction θ_{obj} is given by $k_{obj} = k\sin(\theta_{obj})$.

Fig. 1(c) presents the spatial domain when the separation between receivers (Δx) increases with respect to the previous case. Therefore,

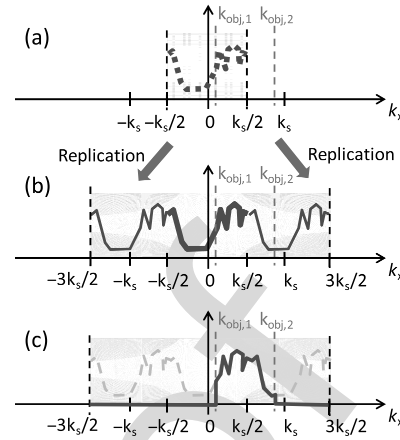

Fig. 3. (a) Plane wave spectrum in the visible $[-k_s/2\ k_s/2]$ interval. (b) Plane wave spectrum replication on the left and right. (c) Plane wave spectrum filtering within the $[k_{obj,1} k_{obj,2}]$ interval.

the spectral domain [Fig. 1(d)] is compressed, which may cause overlapping between spectral replicas.

III. Fourier-Based Imaging for Off-Centered OUT

As stated in Section I, on-the-move personnel screening has to take into account cases in which the OUT is not centered with respect to the receiving array, as shown in Fig. 2(a). Such cases include, e.g., those in which the person is on one side of the system.

In this case, the field of view ranges from $\theta_{obj,1}$ to $\theta_{obj,2}$. In the spectral domain k_x, the values of $k_{obj,1}$ and $k_{obj,2}$ are given by the position of the OUT with respect to the center of the receiving array. Thus, the scattered field plane wave coefficients are within the range $k_{obj,1} = k\sin(\theta_{obj,1})$ to $k_{obj,2} = k\sin(\theta_{obj,2})$, as plotted in Fig. 2(b).

Provided that the receiving array is sampled below the Nyquist criterion, $\Delta x \leq \lambda/2$, even for a limiting case with $\theta_{obj,i} = 90^\circ$($i =$ *1,2*), $k_s/2 \geq k_{obj,i} = k$, and no aliasing will occur.

When $\Delta x > \lambda/2$, the array is subsampled, as shown in Fig. 2(c). If $\Delta x > \pi/(k\sin(\theta_{obj,i})) = \lambda/(2\sin(\theta_{obj,i}))$, then part of the OUT plane wave spectrum will be outside the spectral interval $-k_s/2$ to $k_s/2$, as presented in Fig. 2(d). This means that spectral information will be lost, and the OUT will not be correctly reconstructed. Besides, the adjacent spectral replicas partially lie within the $[-k_s/2 k_s/2]$ interval, as shown in Fig. 2(d) (yellow dashed line).

A new method to recover the information within the interval $[k_{obj,1}\ k_{obj,2}]$ is proposed for cases in which only nonsignificant parts of the spectrum overlap, as plotted in Fig. 2(d). The proposed technique of spectral information recovery consists of three steps, as presented in Fig. 3.

1) From the acquired scattered field, the plane wave spectrum between $[-k_s/2\ k_s/2]$ is calculated [Fig. 3(a)].
2) Because the limits $k_{obj,1}$ and $k_{obj,2}$ are known from the estimated OUT size, the plane wave spectrum is replicated n times (with $n > 0$) on the left and the right side [Fig. 3(b)], satisfying $(-2n-1)k_s/2 < [k_{obj,1}\ k_{obj,2}] < (2n+1)k_s/2$.
3) Finally, a band-pass filter is applied such that only the plane wave spectrum within the $[k_{obj,1}\ k_{obj,2}]$ interval, i.e., the relevant plane wave coefficients for OUT imaging, is maintained [Fig. 3(c)]. The reconstructed image of the OUT is created with the data associated with the filtered plane wave spectrum coefficients.

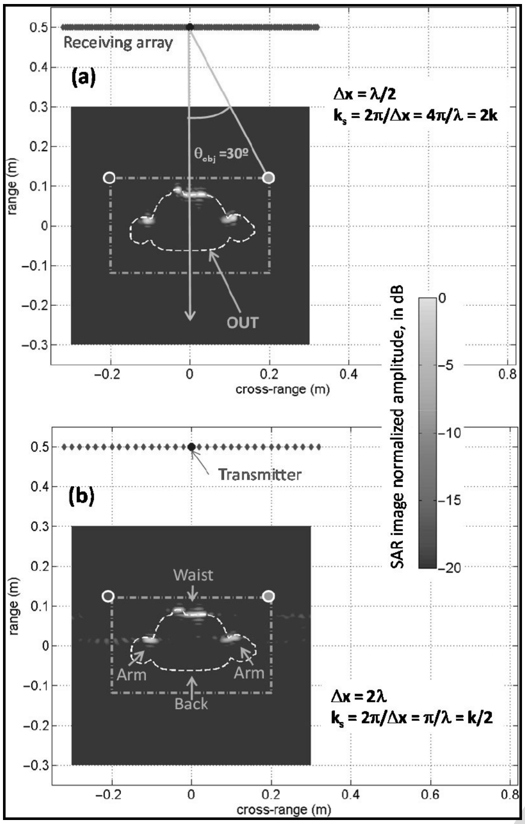

Fig. 4. Setup for mm-wave imaging with a linear receiving array and a point source-like transmitter. The OUT (white dashed line) is centered with respect to the receiving array. (a) Receiving array sampled every $\lambda/2$. (b) Receiving array sampled every 2λ.

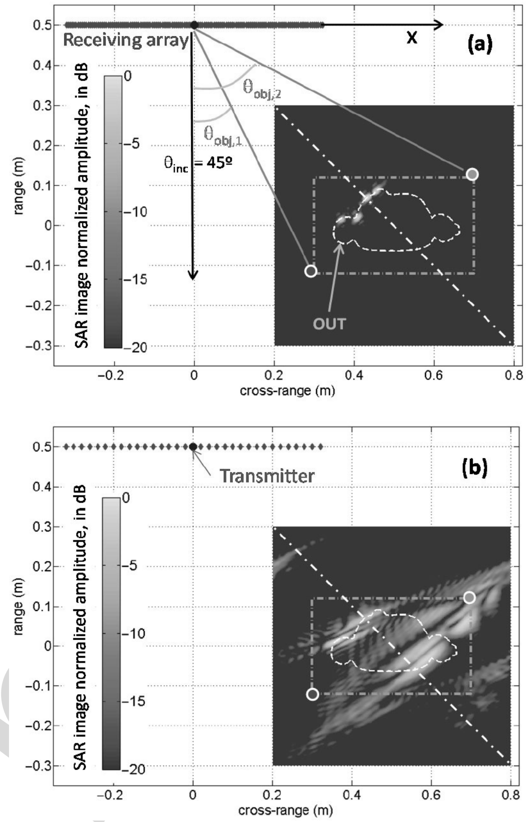

Fig. 6. Setup for mm-wave imaging with a linear receiving array and a point source-like transmitter. The OUT (white dashed line) is displaced 50 cm along the cross-range axis with respect to the receiving array. (a) Receiving array sampled every $\lambda/2$. (b) Receiving array sampled every 2λ.

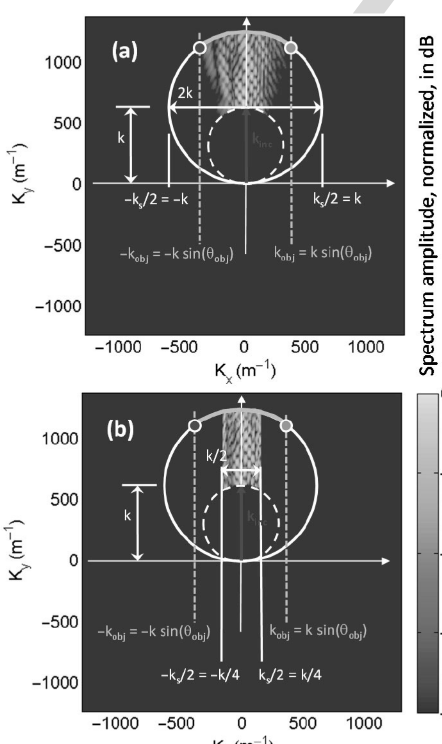

Fig. 5. Plane wave spectrum of the scattered field when the OUT is centered with respect to the receiving array. (a) Receiving array sampled every $\lambda/2$. (b) Receiving array sampled every 2λ.

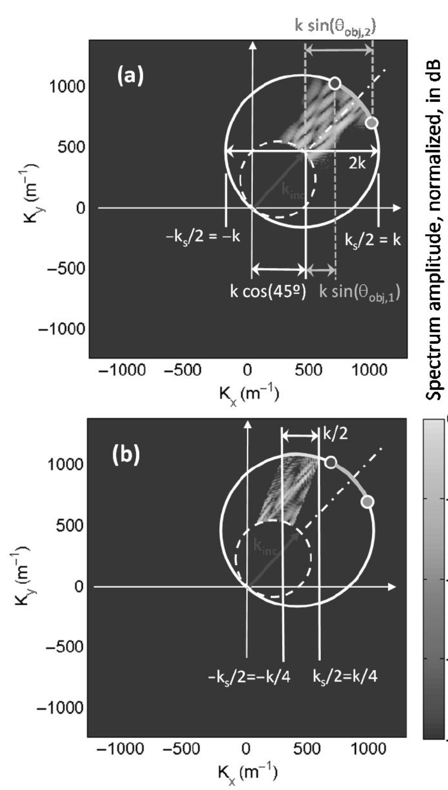

Fig. 7. Plane wave spectrum of the scattered field when the OUT is displaced 50 cm along the x-axis with respect to the receiving array. (a) Receiving array sampled every $\lambda/2$. (b) Receiving array sampled every 2λ.

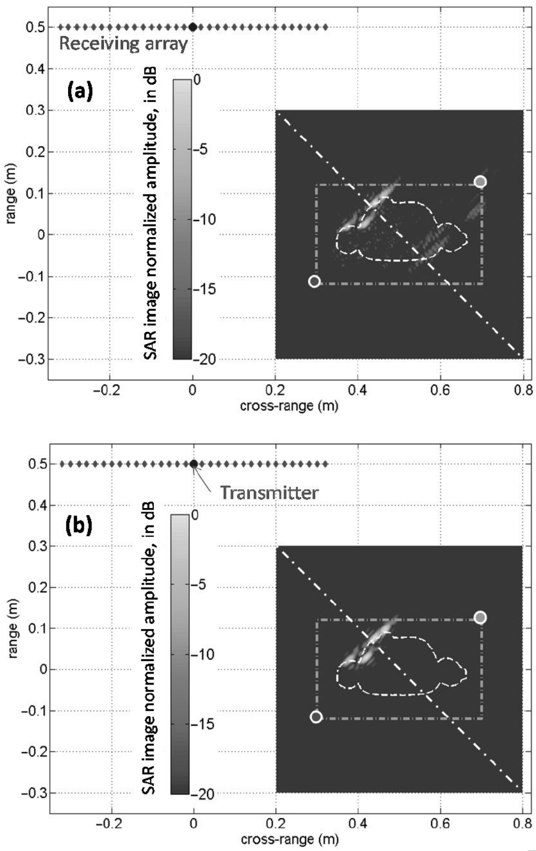

Fig. 8. Setup for mm-wave imaging with a linear receiving array sampled every 2λ and a point source-like transmitter. The OUT (white dashed line) is displaced 50 cm along the cross-range axis with respect to the receiving array. SAR imaging results (a) after spectrum replication and (b) after spectrum replication and filtering.

IV. Application Example

The described methodology is validated through a simulation-based application example. The scattered field is simulated by using the 2-D method-of-moments MATLAB code, which implements electric field integral equations [12].

Fig. 4 presents the imaging setup, which resembles a typical mm-wave imaging system for screening applications: the OUT represents a person's cross-section with an object on the waist. A point source-like transmitter provides illumination, and a linear array of receivers collects the scattered field. Vertical (TM) polarization is considered, with a 15–30 GHz working frequency band.

As described in [11], an on-the-move imaging system takes advantage of the multiple positions of a person to recover the entire profile. To show this concept, two different OUT positions, centered and off-centered with respect to the receiving array, are considered in this example.

For the case in which the OUT is facing the receiving array, the viewing angle is $\theta_{\text{obj}} \leq 30^\circ$.

Fig. 4 presents the imaging results for array sampling rates of $\lambda/2$ [Fig. 4(a)] and 2λ [Fig. 4(b)] at $f = 30$ GHz. The latter image is slightly distorted due to aliasing. The plane wave spectra for these two cases are plotted in Fig. 5(a) and (b), respectively. The correspondence between the spatial and the spectral mapping for the extreme angles $\pm\theta_{\text{obj}}$ are denoted by red (•) and green (•) circles, respectively, in Figs. 4 and 5.

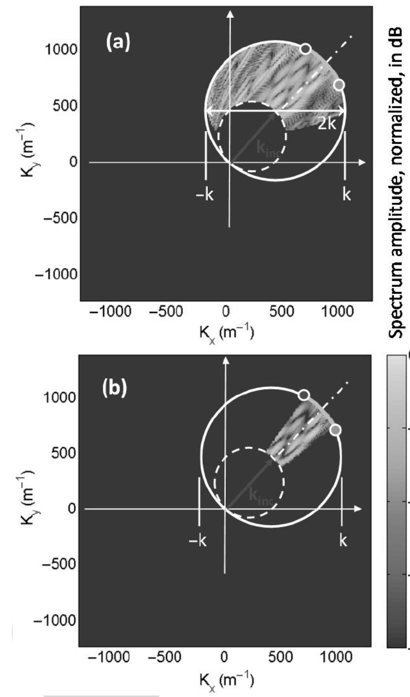

Fig. 9. Plane wave spectrum of the scattered field when the OUT is displaced 50 cm along the x-axis with respect to the receiving array. (a) After spectrum replication. (b) After spectrum replication and filtering.

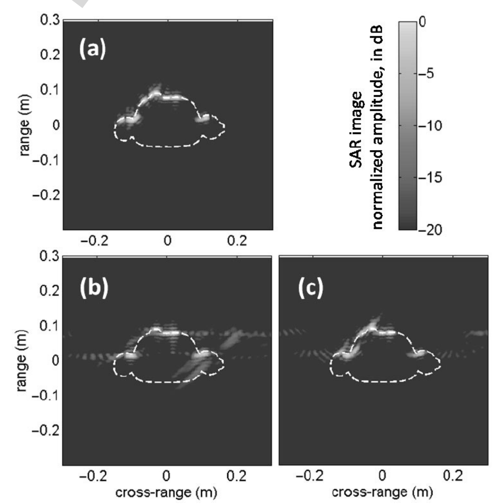

Fig. 10. Combined centered and off-centered SAR images. (a) Receiving array sampled every $\lambda/2$. (b) Receiving array sampled every 2λ. (c) Receiving array sampled every 2λ, applying spectrum replication and filtering.

For the k_{x} and k_{y} coordinates, the k-space mapping is given by [3], [5]

$$k_x = \underbrace{k\sin(\theta_{inc})}_{k_{x,inc}} + k\sin(\theta_{\text{obj}}) \tag{3}$$

$$k_y = \underbrace{k\cos(\theta_{inc})}_{k_{y,inc}} + \sqrt{k^2 - (k\sin(\theta_{\text{obj}}))^2}. \tag{4}$$

The terms $k_{\text{x,inc}}$ and $k_{\text{y,inc}}$ refer to the incident field compensation, with θ_{inc} denoting the incident field angle with respect to the y-(range) axis ($\theta_{\text{inc}} = 0^\circ$ in this case). Multistatic imaging requires that the plane

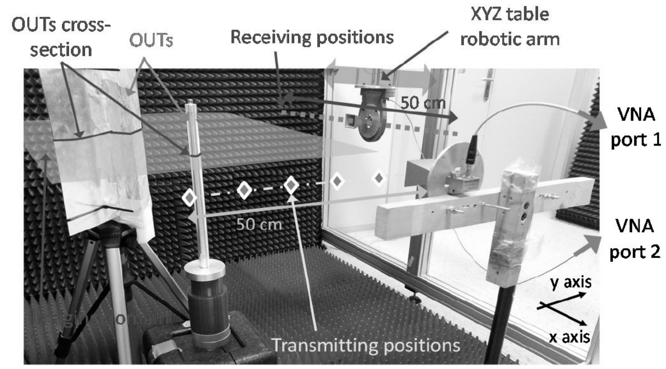

Fig. 11. Ku-band measurement setup for experimental validation. The receiver is mounted on a robotic arm and the transmitter is manually placed at six different positions. The transmitting horn antenna is connected to Port 1 of the vector network analyzer (VNA), and the receiving horn antenna, mounted on the XYZ table robotic arm, to Port 2 of the VNA. Vertical polarization is considered.

wave spectrum be compensated by the incident field. For simplicity, the spherical wave of the incident field can be locally approximated as a plane wave [5]; thus, in the spectral domain, the incident field compensation is a linear shift with magnitude $k_{\text{inc}} = k$ (Fig. 7, red arrow).

When the array is sampled every $\lambda/2$, then $k_{\text{s}}/2 = k$, as shown in Fig. 5(a). In this case, $k_{\text{obj}} = k\sin(30^\circ) = k/2 < k_{\text{s}}/2$. When the distance between consecutive receivers is 2λ, the sampling rate increases according to $k_{\text{s}}/2 = k/4$ [Fig. 5(b)], and $k_{\text{obj}} = k/2 > k_{\text{s}}/2$. This will cause the spectral replicas to overlap and the OUT image to become distorted due to aliasing.

Next, the OUT is displaced 50 cm in the x-direction, as shown in Fig. 6. For a receiving array separation of $\lambda/2$ [Fig. 6(a)], the image does not suffer from aliasing because $k_{\text{s}}/2 = k > \max([k_{\text{obj},1} k_{\text{obj},2}])$. Fig. 7(a) shows the analysis results for this case in the spectral domain. The incident field can be approached by a $\theta_{\text{inc}} = 45^\circ$ incident plane wave; thus, the plane wave spectrum is shifted to $k_{\text{x,inc}} = k\cos(45^\circ)$ and $k_{\text{y,inc}} = k\sin(45^\circ)$ [5]. The correspondence between the spatial and the spectral mapping for the extreme angles $\theta_{\text{obj},1}$ and $\theta_{\text{obj},2}$ are indicated by red (•) and green (•) circles, respectively, in Figs. 6 and 7.

If the sampling rate is lowered to $k_{\text{s}}/2 = k/4$, then the spectral domain will be outside the $[k_{\text{obj},1} k_{\text{obj},2}]$ interval, as shown in Fig. 7(b). As a result, the OUT cannot be imaged, as plotted in Fig. 6(b).

To recover the plane wave spectrum, the methodology presented in Fig. 3 is applied. First, the plane wave spectrum in the $[-k_{\text{s}}/2\ k_{\text{s}}/2]$ interval is replicated twice on the left and twice on the right to cover the $[-5k_{\text{s}}/2 5k_{\text{s}}/2]$ range. After applying the corresponding incident field compensation (k_{inc}), the extended plane wave spectrum is plotted in Fig. 9(a). Now, the condition $-5k_{\text{s}}/2 < [k_{\text{obj},1} k_{\text{obj},2}] < 5k_{\text{s}}/2$ is satisfied. Due to the spectral replicas, the recovered OUT image suffers from aliasing, as shown in Fig. 8(a).

To remove the plane wave spectrum replicas, the band-pass filter $[k_{\text{obj},1}\ k_{\text{obj},2}]$ is applied to the spectral domain [Fig. 9(b)]. Although it is not possible to remove aliasing completely, it should be noted that the main features visible in Fig. 6(a) are also present in the recovered image in Fig. 8(b).

Concerning the practical application of the proposed method to an on-the-move imaging system, the images for different OUT positions can be combined as described in [11] to recover the OUT profile. In this case, only two positions are tested; the results are plotted in Fig. 10. In the case of subsampled arrays, although aliasing cannot be fully removed, the proposed technique allows for accurate OUT profile reconstruction with a reduced number of receiving elements, thus making the mm-wave imaging system simpler in terms of technical and economic effort.

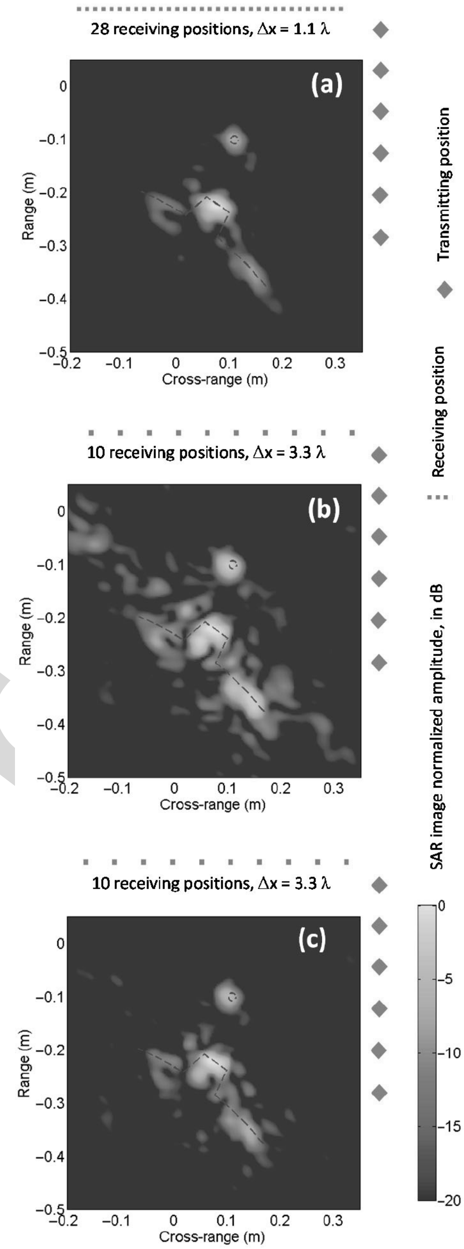

Fig. 12. Combined centered and off-centered SAR images. (a) Receiving array sampled every 1.1λ at 18 GHz. (b) Receiving array sampled every 3.3λ. (c) Receiving array sampled every 3.3λ, applying spectrum replication and filtering. Red dashed line represents the true OUTs profile.

V. Measurements Results

The imaging setup described in Section IV is replicated inside an XYZ table measurement range [13] for practical validation with measurements in the Ku frequency band (12–18 GHz). Fig. 11 shows a picture of the measurement setup. In this setup, the transmitting and receiving positions are located along different sides of the imaging domain, as shown in Figs. 11 and 12, aiming to test the capability of the proposed technique to work with this kind of multistatic imaging setups [5].

Scattered field is measured along a linear synthetic aperture placed at $y = +0.5$ m, ranging from $x = -0.2$ m to $x = +0.3$ m. Six equally spaced transmitting positions, placed at $x = 0.5$ m, and ranging from $y = -0.3$ m to $y = +0.2$ m are considered. The OUTs are a bent metallic plate resembling the cross-section of a human body torso with an object on it, and a 2-cm diameter metallic pole placed at $x = 0.1$ cm, $y = -0.1$ cm, used also as a reference for optical alignment of the transmitter when manually moved from one position to another.

The same process described in Section IV is applied to the measured field samples for every transmitting position. Fig. 12 presents the combined SAR images for all the transmitting positions. Even with a subsampling of 1.1λ [28 receiving positions, Fig. 12(a)] OUTs profile can be recovered without aliasing. However, when the subsampling is increased up to 3.3λ [10 receiving positions, Fig. 12(b)], the recovered image is distorted by aliasing, which can be partially removed after the application of spectrum replication and filtering [Fig. 12(c)].

VI. Conclusion

The limitations of Fourier-based imaging applied to multistatic systems with subsampled arrays were presented and discussed, and a simple technique for partial recovery of plane wave spectrum information was introduced. The simulation and measurement results confirm the viability of the proposed approach in the development of on-the-move multistatic mm-wave imaging systems or any other radar configuration in which the target is off-centered.

References

[1] S. S. Ahmed, A. Schiessl, F. Gumbmann, M. Tiebout, S. Methfessel, and L. Schmidt, "Advanced microwave imaging," *IEEE Microw. Mag.*, vol. 13, no. 6, pp. 26–43, Sep./Oct. 2012.

[2] S. S. Ahmed, "Personnel screening with advanced multistatic imaging technology," in *Proc. SPIE Defense Secur. Sens. Int. Soc. Opt. Photonics*, 2013. Q2

[3] D. M. Sheen, D. L. McMakin, and T. E. Hall, "Three-dimensional millimeter-wave imaging for concealed weapon detection," *IEEE Trans. Microw. Theory Techn.*, vol. 49, no. 9, pp. 1581–1592, Sep. 2001.

[4] D. M. Sheen, D. L. McMakin, and T. E. Hall, "Combined illumination cylindrical millimeter-wave imaging technique for concealed weapon detection," in *Proc. AeroSense Int. Soc. Opt. Photonics*, Jul. 2000, pp. 52–60.

[5] Y. Álvarez *et al.*, "Fourier-based imaging for multistatic radar systems," *IEEE Trans. Microw. Theory Techn.*, vol. 62, no. 8, pp. 1798–1810, Aug. 2014.

[6] G. Yates, M. Horne, A. Blake, R. Middleton, and D. Andre, "Bistatic SAR image formation," *IEE Proc. Radar Sonar Navig.*, vol. 153, no. 3, pp. 208–213, 2006.

[7] M. Soumekh, "Bistatic synthetic aperture radar inversion with application in dynamic object imaging," *IEEE Trans. Signal Process.*, vol. 39, no. 9, pp 2044–2055, Sep. 1991.

[8] X. Zhuge and A. G. Yarovoy, "A sparse aperture MIMO-SAR-based UWB imaging system for concealed weapon detection," *IEEE Trans. Geosci. Remote Sens.*, vol. 49, no. 1, pp. 509–518, Jan. 2011.

[9] B. Gonzalez-Valdes, Y. Alvarez, J. A. Martinez, F. Las-Heras, and C. M. Rappaport, "On the use of improved imaging techniques for the development of a multistatic three-dimensional millimeter-wave portal for personnel screening," *Progr. Electromagn. Res.*, vol. 138, pp. 83–98, 2013.

[10] Y. Rodríguez-Vaqueiro, Y. Álvarez, B. Gonzalez-Valdes, J. A. Martínez-Lorenzo, F. Las-Heras, and C. M. Rappaport, "On the use of compressed sensing techniques for improving multistatic millimeter-wave portal-based personnel screening," *IEEE Trans. Antennas Propag.*, vol. 62, no. 1, pp. 494–499, Jan. 2014.

[11] B. Gonzalez-Valdes, C. Rappaport, and J. A. Martinez-Lorenzo, "On-the-move active millimeter wave interrogation system using a hallway of multiple transmitters and receivers," in *Proc. IEEE Int. Symp. Antennas Propag.*, Memphis, TN, USA, Jul. 6–11, 2014, pp. 1107–1108.

[12] C. A. Balanis, *Advanced Engineering Electromagnetics*. Hoboken, NJ, USA: Wiley, 1989.

[13] A. Arboleya, Y. Alvarez, and F. Las-Heras, "Millimeter and submillimeter planar measurement setup," in *Proc. IEEE Antennas Propag. Soc. Int. Symp. (APS-URSI)*, Orlando, FL, USA, Jul. 7–13, 2013, pp. 1–2.

QUERIES

Q1: Please confirm whether the edit made in the sentence “This communication...” is correct.
Q2: Please provide page range for Ref. [2].